Article

CO2 Methanation over Ni Catalysts Supported on Prdoped CeO2 Nanostructures Synthesized via Hydrothermal and Coprecipitation Methods

Anastasios I. Tsiotsias , Nikolaos D. Charisiou * , Aasif A. Dabbawala , Aseel G.S. Hussien , Victor Sebastian , Steven Hinder , Mark Baker , Samuel Mao , Kyriaki Polychronopoulou , Maria Goula *

Posted Date: 22 May 2025

doi: 10.20944/preprints202505.1794.v1

Keywords: CO2 methanation; synthesis method; Pr-doped CeO2; hydrothermal; coprecipitation; nanostructures

 doi:10.20944/preprints202505.1794.v1

Article

CO_2 Methanation over Ni Catalysts Supported on Pr-Doped CeO_2 Nanostructures Synthesized via Hydrothermal and co-Precipitation Methods

Anastasios I. Tsiotsias [1], Nikolaos D. Charisiou [1,*], Aasif A. Dabbawala [2,3], Aseel G.S. Hussien [2,3], Victor Sebastian [4,5,6], Steven J. Hinder [7], Mark A. Baker [7], Samuel Mao [2], Kyriaki Polychronopoulou [2,3] and Maria A. Goula [1,8,9,*]

[1] Laboratory of Alternative Fuels and Environmental Catalysis (LAFEC), Department of Chemical Engineering, University of Western Macedonia, GR-50100, Kozani, Greece
[2] Department of Mechanical Engineering, Khalifa University of Science and Technology, Abu Dhabi, P.O. Box 127788, UAE
[3] Center for Catalysis and Separations, Khalifa University of Science and Technology, Abu Dhabi, P.O. Box 127788, UAE
[4] Department of Chemical Engineering and Environmental Technology, Universidad de Zaragoza, Campus Río Ebro-Edificio I+D, 50018 Zaragoza, Spain
[5] Instituto de Nanociencia y Materiales de Aragón (INMA), Universidad de Zaragoza- CSIC, c/ María de Luna 3, 50018 Zaragoza, Spain
[6] Networking Research Center on Bioengineering, Biomaterials and Nanomedicine, CIBERBBN, 28029 Madrid, Spain
[7] The Surface Analysis Laboratory, Faculty of Engineering and Physical Sciences, University of Surrey, Guildford, GU2 4DL, UK
[8] Centre for Research & Technology Hellas (CERTH), Chemical Process and Energy Resources Institute (CPERI), 52 Egialias Str., Maroussi, Athens 15125, Greece
[9] School of Science and Technology, Hellenic Open University, Parodos Aristotelous 18, Patras 26335, Greece
* Correspondence: author: ncharisiou@uowm.gr (N.D.C.); mgoula@uowm.gr (M.A.G.)

Abstract: The synthesis method of the Pr-doped CeO_2 catalyst support in Ni/Pr-CeO_2 CO_2 methanation catalysts is varied by changing the type/ basicity of the precipitating solution and the hydrothermal treatment temperature. The use of highly basic NaOH as the precipitating agent and elevated hydrothermal treatment temperature (100 or 180 ^oC) leads to the formation of structured Pr-doped CeO_2 nanorods and nanocubes, respectively, whereas the use of a mildly basic NH_3-based buffer in the absence of hydrothermal treatment (i.e., co-precipitation) leads to an unstructured mesoporous morphology with medium-sized supported Ni nanoparticles. The latter catalyst (Ni/CP_NH3) displays a high surface area, high population of moderately strong basic sites, and favorable Ni dispersion. These properties lead to a higher catalytic activity for CO_2 methanation (75% CO_2 conversion and 99% CH_4 selectivity at 350 ^oC) compared to the catalysts with structured nanorod and nanocube support morphologies, which are found to contain a significant amount of leftover Na from the synthesis procedure that can act as a catalyst inhibitor. In addition, the best-performing Ni/CP_NH3 catalyst is shown to be highly stable, with minimal deactivation during time-on-stream operation.

Keywords: CO_2 methanation; Synthesis method; Pr-doped CeO_2; Hydrothermal; Co-precipitation; Nanostructures

 doi:10.20944/preprints202505.1794.v1

1. Introduction

The swift increase in anthropogenic CO_2 emissions risks disrupting the Earth's climate, since CO_2 functions as a greenhouse gas leading to a steep rise in the atmospheric temperature [1,2]. To keep its concentration in check, it is crucial to develop effective carbon capture and storage, as well as carbon capture and utilization technologies, the latter of which can result in the generation of value-added products from waste CO_2 streams [3–5]. On the other hand, the fluctuating nature of renewable energy production necessitates long-term energy storage solutions, which can be achieved through chemical energy storage in the form of "green" hydrogen that is produced through electrolysis [6]. However, hydrogen has a low volumetric energy density, presenting challenges for its effective storage and transportation [7]. To this end, the produced green hydrogen can be used to hydrogenate the captured CO_2 to generate CH_4 (synthetic natural gas), which presents a much higher energy density, as well as easier storage and transportation options, via the CO_2 methanation reaction (Eq. 1) [8–10].

$$CO_2 + 4H_2 \rightarrow CH_4 + 2H_2O \quad (1)$$

Noble metal catalysts like Rh and Ru have demonstrated significant catalytic activity for this particular reaction [9–11]. However, their prohibitively high cost remains a considerable limitation, leading to the widespread use of alternative, transition metal catalysts, particularly Ni-based ones [12,13]. Ni catalysts supported on CeO_2-based supports are known for their superior CO_2 methanation catalytic activity when compared to those supported on other metal oxide supports (e.g., Al_2O_3, SiO_2, or ZrO_2), which is ascribed to the rich defect chemistry and high oxygen vacancy population/ oxygen mobility of the CeO_2 lattice, facilitating the rapid conversion and removal of intermediate species [13–15]. The doping of CeO_2 with trivalent cations, like La^{3+} [16], Sm^{3+} [17], and Pr^{3+} [18–20], has also been shown to significantly enhance the oxygen vacancy population (to charge-balance the extrinsic substitutional defects) and improve the CO_2 methanation catalytic activity. Particularly, in our previous work [20], we found that the Pr-doping of the CeO_2 support at 10 mol% can provide the maximum promoting effect for Ni-supported CO_2 methanation catalysts.

In recent years, many research studies have focused on the hydrothermal synthesis of CeO_2-based nanostructures with varying morphologies and exposed crystalline facets [21–27]. The hydrothermal synthesis utilizing a highly basic/ concentrated NaOH solution as the precipitating agent has been frequently employed for this purpose, with variations in the hydrothermal treatment temperature typically leading to the formation of nanorods, nanocubes, or other metal oxide support nanostructures [21,22,24–26]. For example, Hashimoto et al. [21] demonstrated that a Ni catalyst supported on hydrothermally prepared CeO_2 with nanorod morphology exhibited a higher catalytic activity when compared to those supported on CeO_2 with nanocube and nanooctahedral morphology, which was attributed to the enhanced surface oxygen reactivity of the (110) facet of crystalline CeO_2. Similar findings have also been reported by Bian et al. [22] and Ma et al. [23]. Conversely, according to Jomjaree et al. [24], Ni supported on CeO_2 nanopolyhedrons, and according to Bian et al. [25], Ni supported on CeO_2 nanoparticles, both prepared using more diluted/ less basic NaOH precipitating solutions, were superior compared to Ni supported on nanorod and nanocube CeO_2 support morphologies. The utilization of precipitating solutions with a weaker basicity during hydrothermal synthesis remains considerably less common in the literature. Furthermore, co-precipitation synthesis for the CeO_2-based support, which often proceeds similarly to hydrothermal synthesis (but without the hydrothermal treatment step at an autoclave), has also been employed in a number of studies [28–30], but it generally receives significantly less attention compared to the hydrothermal synthesis, and these similar preparation techniques are rarely compared with each other.

Therefore, in this work, we perform a comparative study by altering the support synthesis method (Pr-doped CeO_2) in Ni-based catalysts via the variation of two synthesis parameters: i) the basicity of the precipitating solution (highly basic NaOH vs mildly basic NH_3-based buffer) and ii)

 doi:10.20944/preprints202505.1794.v1

the hydrothermal treatment temperature (100 °C, 180 °C, or room temperature, i.e., co-precipitation). The doping of the CeO_2 support with 10 mol% Pr was performed to enhance the activity of the corresponding catalysts based on the results of our prior work [20]. It is found that the use of a mildly basic NH_3-based buffer in the absence of hydrothermal treatment (co-precipitation) leads to an unstructured mesoporous support morphology that provides a significantly higher catalytic activity during CO_2 methanation. This can be attributed to favorable physicochemical properties such as a high surface area, high basic site population of moderate strength, suitable Ni dispersion, and the absence of leftover Na that can act as catalyst inhibitor. As such, the rather simpler co-precipitation support synthesis with a mildly basic precipitating agent can yield better catalytic results when compared to the preparation of structured supports with nanorod and nanocube morphologies using highly basic NaOH.

2. Materials and Methods

2.1. Synthesis Methods

Pr-doped CeO_2 nanostructures (10 mol% Pr nominal composition, or $Ce_{0.9}Pr_{0.1}O_{2-\delta}$) were synthesized via several hydrothermal and co-precipitation synthesis methods, by varying the precipitating agent, i.e., the basicity of the precipitating solution during the hydrothermal/ co-precipitation synthesis, and the temperature of the hydrothermal treatment (Table 1).

When NaOH was used as the precipitating agent (high basicity of the precipitating solution, pH > 14), the following procedure was followed: At first, $Ce(NO_3)_3{\cdot}6H_2O$ (Aldrich, 99%) and $Pr(NO_3)_3{\cdot}6H_2O$ (Aldrich, 99.9%) in calculated amounts were dissolved in 50 ml of d-H_2O in a beaker under stirring. In another beaker, NaOH (Fluka, K ≤0.02%, pellets) was added in 150 ml of d-H_2O, so that the final concentration of NaOH (200 ml final solution) would be 10 M. The two solutions were then mixed together, and the final mixture was stirred for another 30 min and then transferred to a 300 ml Teflon-lined stainless-steel autoclave. Two hydrothermal treatment protocols were used: In the first one, the temperature was increased up to 100 °C (NaOH_100), and in the second one up to 180 °C (NaOH_180). In both cases, the mixture remained at that temperature for 24 h. A further co-precipitation protocol was performed, where the final mixture was kept at room temperature for 24 h without undergoing any hydrothermal treatment (CP_NaOH).

When an NH_3-based buffer (NH_3/$(NH_4)_2CO_3$) was used as the precipitating agent (low basicity of the precipitating solution, pH = 9), the following procedure was followed: At first, calculated amounts of the metal nitrates of Ce and Pr were dissolved in 100 ml of d-H_2O under stirring. The pH was then adjusted to 9 via the dropwise addition of a buffer solution of 3 M NH_3/$(NH_4)_2CO_3$. The volume was then increased to 200 ml (pH remaining at 9) via the further addition of d-H_2O and some buffer solution. The final mixture was stirred for 30 min and then transferred to a 300 ml Teflon-lined stainless-steel autoclave. Two hydrothermal treatment protocols were used: In the first one, the temperature was increased up to 100 °C (NH3_100), and in the second one up to 180 °C (NH3_180). In both cases, the mixture remained at that temperature for 24 h. A further co-precipitation protocol was performed, where the final mixture was kept at room temperature for 24 h without undergoing any hydrothermal treatment (CP_NH3).

In all cases, after the 24 h treatment at either room temperature, 100 °C, or 180 °C, the final mixtures were centrifuged, the recovered solids were then washed thoroughly with d-H_2O and once with ethanol, then dried at 70 °C overnight and afterwards calcined at 500 °C for 4 h under static air to prepare the corresponding Pr-doped CeO_2 support oxides with varying nanostructures.

Wet impregnation was then used to introduce the catalytically active Ni phase. At first, $Ni(NO_3)_2{\cdot}6H_2O$ (Fluka, 97%), for a final Ni loading of 10 wt%, was added in 100 ml of d-H_2O. The metal oxide support powder was then added to the solution under stirring. Afterwards, the water was removed in a rotary evaporator at 72 °C and the leftover slurry was overnight dried at 90 °C, and then calcined at 400 °C for 4h to obtain the calcined catalysts (NiO/ Support). To prepare the

 doi:10.20944/preprints202505.1794.v1

corresponding reduced catalysts (Ni/ Support), the calcined ones were reduced under H_2 flow at 500 °C for 1 h.

Table 1. Overview of the different precipitating agents and hydrothermal treatments used to prepare each Pr-doped CeO_2 metal oxide support.

Catalyst support	Precipitating agent	Hydrothermal treatment temperature
CP_NaOH	NaOH	R.T. [1] (Co-precipitation)
HT_NaOH_100	NaOH	100 °C
HT_NaOH_180	NaOH	180 °C
CP_NH3	NH_3/ $(NH_4)_2CO_3$	R.T. [1] (Co-precipitation)
HT_NH3_100	NH_3/ $(NH_4)_2CO_3$	100 °C
HT_NH3_180	NH_3/ $(NH_4)_2CO_3$	180 °C

[1] R.T. = Room Temperature.

2.2. Characterization Techniques

X-ray diffraction (XRD) was performed on a MiniFlex II Rigaku powder diffractometer, using a Cu-$K_{\alpha 1}$ radiation source at 30 kV and 20 mA. To calculate the crystallite sizes of each phase, the Scherrer equation was applied on the strongest reflection.

N_2 physisorption (adsorption/desorption) was carried out on a 3Flex instrument (Micromeritics) at 77K. The specific surface area (SSA, m^2/g) was determined via the multi-point Brunauer-Emmet-Teller (BET) method for $0.05 < P/P^\circ < 0.20$, and the pore size distribution (PSD) via the Barrett–Joyner–Halenda (BJH) theory.

H_2-temperature programmed reduction (H_2-TPR) and CO_2-temperature programmed desorption (CO_2-TPD) were performed on an Autochem 2920 instrument (Micromeritics). For H_2-TPR on the calcined catalysts, the samples were first treated under 20% O_2/He at 500 °C for 2 h and then cooled down to ambient temperature. Afterwards, 10% H_2/Ar was passed through the materials during the temperature ramp (30 °C/min). For CO_2-TPD on the reduced catalysts, the samples were first treated under H_2 flow at 500 °C for 2 h. Afterwards, 10% CO_2/He was flown at room temperature for the CO_2 adsorption. The temperature was then increased with a 30 °C/min ramp under He flow. In both cases, the thermal conductivity detector (TCD) signal was continuously recorded during the temperature ramp.

X-ray photoelectron spectroscopy (XPS) was performed on a ThermoFisher Scientific K-Alpha+ instrument using a monochromated Al K_a X-ray source (1486.6 eV), with a 400 μm radius X-ray spot. 200 eV pass energy was employed for the survey spectra and 50 eV for the core level spectra (higher resolution). Instrument modified sensitivity factors were used for quantification. The adventitious carbon C1s peak at 285.0 eV was used for charge referencing.

Lastly, transmission electron microscopy (TEM) was performed on a G2 20 S-Twin Tecnai microscope featuring a LaB_6 electron source and a "SuperTwin®" objective lens that allows point-to-point resolution of 0.24 nm. High-angle annular dark field scanning transmission electron microscopy (STEM–HAADF) along with energy dispersive X-ray spectroscopy (EDS) analysis were carried out on an Analytical Titan (FEI) field emission gun microscope (300 kV), featuring a Cs-probe that allows electron probe formation of 0.09 nm (CEOS).

2.3. Catalytic Testing

Catalytic testing was carried out at ambient pressure in a fixed-bed quartz reactor (I.D. = 0.9 cm), with a similar procedure as that described in Ref. [31]. All catalysts were previously reduced in-situ for 1 h at 500 °C under H_2 flow. The catalytic performance was evaluated using three experimental protocols (#1, #2, and #3) under a continuous-flow gas feed of: 10% CO_2, 40% H_2, balance Ar, 100 ml/min total flow.

 doi:10.20944/preprints202505.1794.v1

In short, under Experimental Protocol #1, the catalytic activity was studied as a function of reaction temperature under a relatively low WHSV of 25,000 ml g_{cat}^{-1} h^{-1}. The temperature of the reactor was gradually increased via 50 °C steps from 200 °C up to 450 °C.

Under Experimental Protocol #2, a higher WHSV of 100,000 ml g_{cat}^{-1} h^{-1} was employed, along with additional temperature steps every 10 °C from 250 °C up to 350 °C. The activation energy was calculated via this experimental protocol, making the assumption of pseudo-first order reaction kinetics and for low values of CO_2 conversion (< 20%), to negate the influence of mass transfer.

Under Experimental Protocol #3, the catalysts were evaluated regarding their stability during time-on-stream testing for 24 h at a constant temperature of 350 °C (WHSV = 25,000 ml g_{cat}^{-1} h^{-1}, as in Experimental Protocol #1).

The gases exiting the reactor were analyzed online by a gas chromatography analysis system, as described in Ref. [18]. Besides CH_4, CO was the sole hydrogenation by-product detected. Deviations calculated for the carbon balance were limited to ±3%. The following Eqs. 2-4 were used in order to calculate the reaction metrics (CO_2 conversion, CH_4 selectivity, and CH_4 yield):

$$X_{CO_2}(\%) = \frac{C_{CH_4}^{out} + C_{CO}^{out}}{C_{CO_2}^{out} + C_{CH_4}^{out} + C_{CO}^{out}} \cdot 100 \quad (2)$$

$$S_{CH_4}(\%) = \frac{C_{CH_4}^{out}}{C_{CH_4}^{out} + C_{CO}^{out}} \cdot 100 \quad (3)$$

$$Y_{CH_4}(\%) = \frac{X_{CO_2} \cdot S_{CH_4}}{100} \quad (4)$$

where C^{out} is the molar concentration at the reactor outlet for each gas.

Lastly, Eq. 5 was used to calculate the consumption rate of CO_2 (mol g_{cat}^{-1} s^{-1}):

$$r_{CO_2} = \left(\frac{X_{CO_2}}{100}\right) \cdot \left(\frac{F_{CO_2}}{W_{cat}}\right) \quad (5)$$

where X_{CO_2} is the conversion of CO_2 (%), F_{CO_2} is the molar flow rate of CO_2 entering the reactor (mol s^{-1}), and W_{cat} is the catalyst mass (g).

3. Results and Discussion

3.1. Characterization of the Supports and the Ni Catalysts

At first, the prepared Pr-doped CeO_2 metal oxide supports and the corresponding Ni-supported catalysts were characterized via XRD (Figure 1a,b). The Pr-doped CeO_2 supports (Figure 1a) present the typical diffractions of the fluorite CeO_2 lattice with a different peak broadening [18,20]. The calculated average crystallite sizes via the Scherrer equation fall in the range between 8-10 nm (Table 2), except for the HT_NaOH_180 support, which has an average crystallite size of around 20 nm. Therefore, the high basicity of the precipitating agent coupled with a high temperature for the hydrothermal treatment (180 °C) appear to favor the lattice growth of the Pr-doped CeO_2 nanocrystallites.

The reduced Ni-supported catalysts were characterized next (Figure 1b). Besides the diffractions for the Pr-doped CeO_2 support, diffractions attributed to metallic Ni^0 are now also evident due to the presence of the supported Ni nanoparticles [20]. The calculated crystallite sizes for metallic Ni are between 8 and 15 nm (Table 2). The lowest crystallite size was calculated for Ni/HT_NaOH_100 (8 nm) and the highest for Ni/HT_NaOH_180 and Ni/CP_NaOH (15 and 14 nm, respectively). The catalysts whose support was prepared with mildly basic NH_3-based buffer as the precipitating agent have a rather similar Ni dispersion and crystallite size (11-13 nm), i.e., medium-sized Ni nanoparticles.

 doi:10.20944/preprints202505.1794.v1

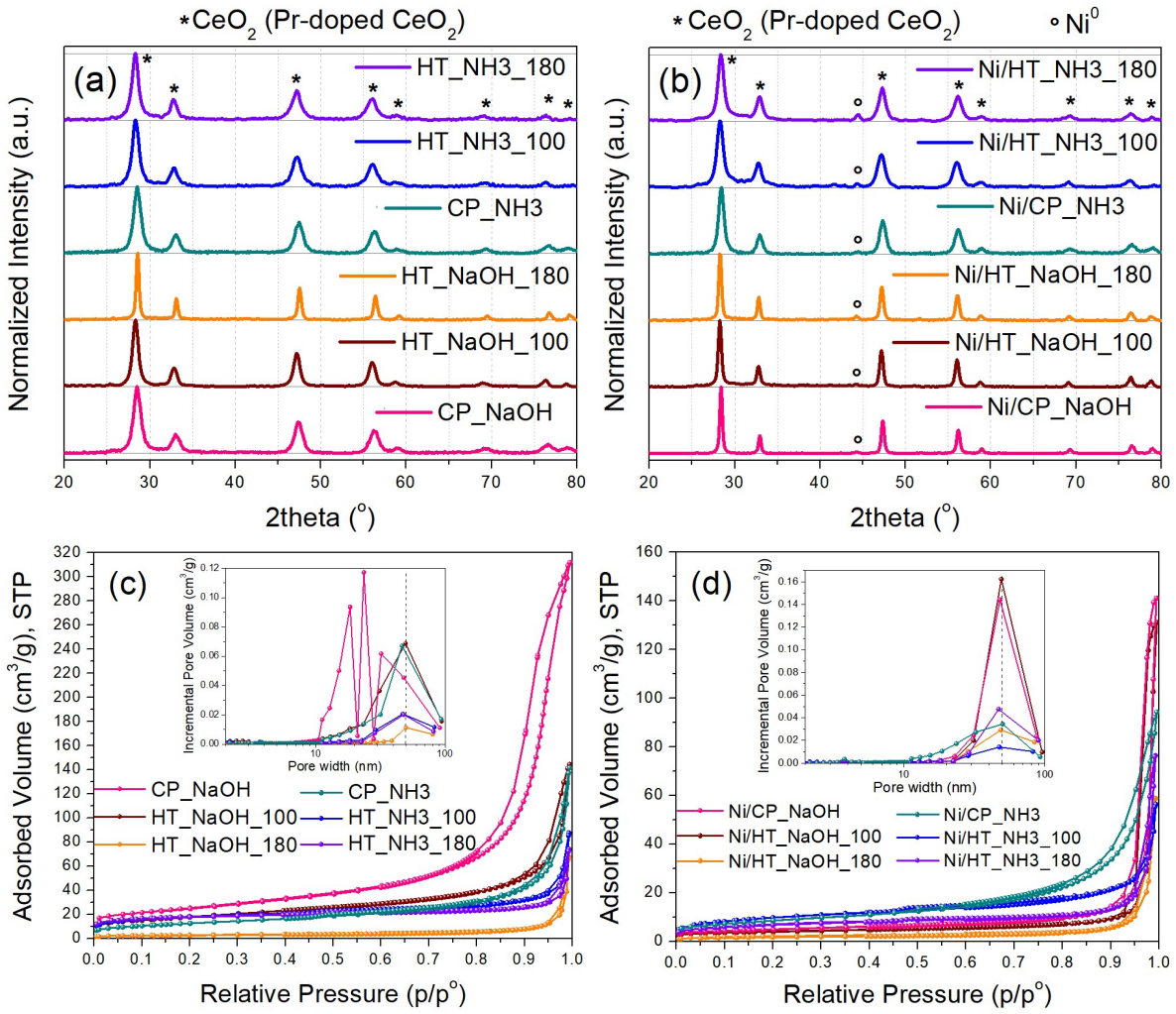

Figure 1. X-ray diffractograms of (**a**) the metal oxide supports and (**b**) the reduced Ni-supported catalysts. N_2 physisorption isotherms along with pore size distribution (inset) of (**c**) the metal oxide supports and (**d**) the reduced Ni-supported catalysts.

It is also interesting to note, that the diffraction broadening of the Pr-doped CeO_2 crystallites changes in some cases from the supports to the reduced catalysts, namely for the Ni/HT_NaOH_100 and especially for the Ni/CP_NaOH catalyst. As a result, all the Ni-supported reduced catalysts prepared via NaOH as the precipitating agent display an almost double average crystallite size for Pr-doped CeO_2 compared to those with NH_3-based buffer as the precipitating agent. To elucidate the origin of this crystal growth in these cases, the calcined Ni-supported catalysts were also characterized (Figure S1), which display the crystalline diffractions for the support crystallites and the oxidized NiO particles. Since the peak broadening for Pr-doped CeO_2 is similar between the bare supports and the calcined catalysts, it can be stated that the Pr-doped CeO_2 crystallite growth in Ni/CP_NaOH and Ni/HT_NaOH_100 occurs during the following high-temperature (500 °C) reduction treatment under H_2.

Afterwards, N_2 physisorption isotherms were collected for the bare supports, as well as for the reduced Ni-supported catalysts (Figure 1c,d). The supports (Figure 1c) display a different porous structure for each material depending on the synthesis method. Most of them are mesoporous with a surface area ranging from 46 up to 93 m^2/g (Table 2), with the highest surface area being recorded for the CP_NaOH sample, which also displays the highest pore volume. An outlier is HT_NaOH_180, which has much larger pore sizes and displays a quite small surface area of just 10 m^2/g.

Regarding the reduced Ni-supported catalysts (Figure 1d), a general trend is that upon Ni impregnation/ calcination followed by reduction, the pore volume and the surface area both drop, while the pore size distribution is shifted towards larger pore diameters. This is a result of the

 doi:10.20944/preprints202505.1794.v1

blocking of the smaller mesopores and pore reconstruction caused by the impregnation of Ni and the formation of supported metallic Ni nanoparticles [31,32]. For the cases of Ni/HT_NaOH_100 and especially Ni/CP_NaOH, a much higher extent of surface area loss occurs (even up to 80%), which is also consistent with the changes in the material crystallinity following Ni impregnation/ calcination and reduction (i.e., significant growth of the Pr-doped CeO_2 crystallites) observed during the XRD characterization. Overall, among all of the Ni-supported reduced catalysts, higher porosity is observed for those whose supports were prepared via the mildly basic NH_3-based buffer as the precipitating agent.

Table 2. Crystallite sizes of CeO_2 (Pr-doped CeO_2, Φ_{CeO2}) and Ni^0 (Φ_{Ni}) calculated from XRD through the Scherrer equation. Specific surface area (SSA), pore volume (V_P), and average pore diameter (D_{ave}) determined via N_2 physisorption. The values are for the reduced Ni-supported catalysts, while those for the respective metal oxide supports can be found in parentheses.

Catalyst	Φ_{CeO_2} (nm)	Φ_{Ni^0} (nm)	SSA (m^2/g)	V_P (cm^3/g)	D_{ave} (nm)
Ni/CP_NaOH	22 (8)	15	17 (91)	0.22 (0.48)	50 (21)
Ni/HT_NaOH_100	17 (10)	8	13 (63)	0.20 (0.22)	61 (14)
Ni/HT_NaOH_180	20 (20)	14	8 (10)	0.09 (0.10)	48 (38)
Ni/CP_NH3	11 (8)	11	31 (46)	0.14 (0.21)	19 (18)
Ni/HT_NH3_100	9 (9)	13	35 (61)	0.08 (0.12)	10 (8)
Ni/HT_NH3_180	10 (9)	13	24 (58)	0.12 (0.11)	19 (7)

The catalyst material reducibility was investigated through H_2-TPR on the calcined Ni-supported catalysts (Figure 2a). At the first region (I), below 200 °C, the observed reduction peaks could be ascribed to the reduction of highly dispersed NiO species at the catalyst surface, as well as possibly to $Ni(OH)_2$ species, and Ni^{2+} solubilized in the Pr-doped CeO_2 support [31,33]. At the second region (II), up to approx. 400 °C, the main (highest intensity) reduction peak can be assigned to the majority of NiO reduction to metallic Ni^0, as well as to the contribution of removal of surface oxygen species from the Pr-doped CeO_2 support [31,33,34]. The peak of the main NiO reduction event is located between 290 – 300 °C for all materials, except for the NiO/HT_NaOH_180, whose NiO reduction peak has a maximum at approx. 330 °C. This temperature range of NiO reduction to metallic Ni^0 can be attributed to the high reducibility of NiO that is in contact with the defect-rich Pr-doped CeO_2 support surface [31,35]. Lastly, the much smaller and quite broad peaks at higher reduction temperatures (region III) can be ascribed to oxygen removal from the bulk of the metal oxide support [31,33,34].

The surface basicity is then evaluated via CO_2-TPD for the reduced Ni-supported catalysts (Figure 2b), which shows three types of desorption peaks. The peaks at lower temperatures can be assigned to weakly-bound carbonates and bicarbonates on the weak basic sites of the materials. The CO_2 desorption peaks at the intermediate temperature range (approx. between 150 °C and 400 °C) are ascribed to carbonates that are formed over the moderately-strong basic sites, whereas the small and broad peaks at higher temperatures are due to the strong basic sites [31,36,37]. Although some materials present quite intense CO_2 desorption peaks at the lower temperature range, Ni/CP_NH3 is found to contain the highest amount of moderately-strong basic sites at intermediate desorption temperatures. Based on the relevant literature [36,38,39], a higher population of moderately-strong basic sites can be associated with a higher catalytic activity during CO_2 methanation, since they act to enhance the CO_2 chemisorption and activation during the catalytic reaction.

 doi:10.20944/preprints202505.1794.v1

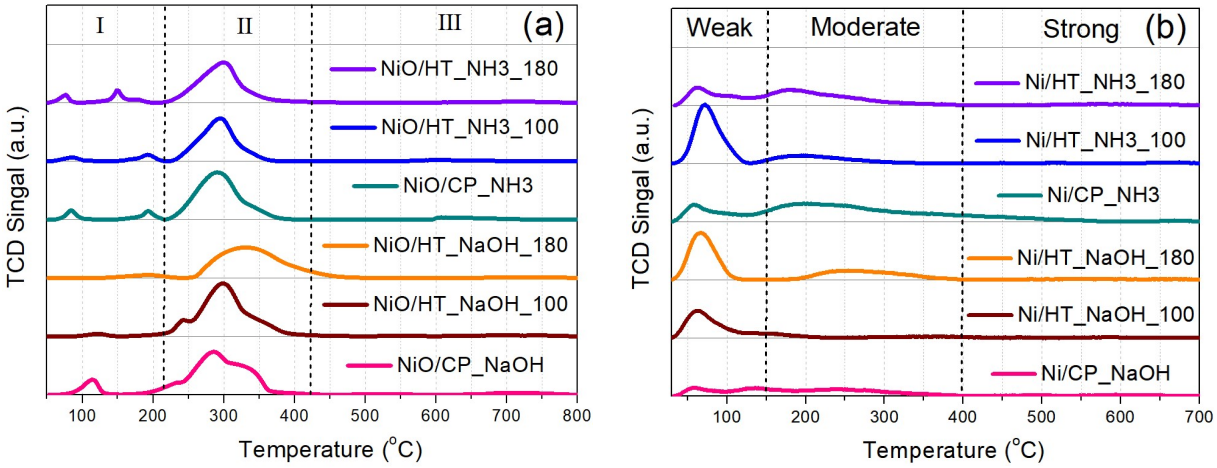

Figure 2. (**a**) H_2-TPR profiles of the calcined catalysts. (**b**) CO_2-TPD profiles of the reduced catalysts.

The catalysts' surface chemistry was studied via XPS, which was conducted ex-situ (Figure 3). The Ni2p spectra (Figure 3a) reveal the following types of surface Ni-species, with increasing binding energy (BE): i) metallic Ni^0 surface sites at lower BE, ii) then NiO surface sites which originate following ex-situ oxidation of formerly metallic surface Ni sites and iii) finally, at higher BE, the large peak can be ascribed to the contribution of $Ni(OH)_2$, which can arise following surface Ni oxidation and hydroxylation, Ni_2O_3 or Ni^{3+} due to defects in the NiO structure, and Ni species at the Ni-CeO_2 interface (Ni-O-Ce sites) [20,34,40]. Regarding the O1s spectra (Figure 3b), these can be separated into surface oxygen from the metal oxide support lattice (Pr-doped CeO_2) at lower BE, and adsorbed oxygen species, like hydroxyls and carbonates on the catalyst surface, and also physisorbed H_2O, at higher BE [20,41]. The majority of these adsorbed oxygen species at higher BE are also expected to originate following atmospheric exposure [20]. Although differences in the peak shapes are observed for the different catalysts, these can be rather attributed to the exposure of the samples to atmospheric oxygen, and to a different extent of surface oxidation and hydroxylation. In particular, the entirety of the Ni phase is expected to be initially metallic following the reduction treatment at 500 °C, as was verified during H_2-TPR characterization (Figure 2a), and thus, the oxidized Ni species in the materials originate during the subsequent atmospheric exposure.

The Ce3d spectra (Figure 3c) show the presence of multiple peaks due to the $Ce3d_{5/2}$ (peaks labeled as v) and $Ce3d_{3/2}$ (peaks labeled as u) transitions. Since Ce ions typically exist in both Ce^{4+} and Ce^{3+} oxidation states in CeO_2-based oxides, the peaks v, v′′, v′′′, u, u′′ and u′′′ can be ascribed to the major Ce^{4+} oxidation state, whereas the peaks v′ and u′ correspond to the minority Ce^{3+} ions due to intrinsic defects in the oxide support lattice [18,20]. However, the majority of the oxygen vacancy sites are expected to originate via the extrinsic substitutional defects of aliovalent Pr^{3+} ions in former Ce^{4+} sites [20,42]. In the Pr3d spectra (Figure 3d), the position and peak shape of the $Pr3d_{5/2}$ and $Pr3d_{3/2}$ transition peaks resemble those of a Pr_2O_3-like oxide, thus confirming that Pr rather exists in the Pr^{3+} oxidation state [20,43]. These extrinsic (Pr_{Ce}') substitutional defects can generate a large number of oxygen vacancy sites, which can significantly promote the CO_2 methanation catalytic activity [14,15,33].

The elemental surface concentrations measured via XPS can be found in Table S2. The differences in adventitious carbon and the surface concentration of some elements can be attributed to atmospheric exposure, although they roughly agree with the expected values. A more pronounced Ni concentration at the surface is expected, since Ni is mainly located as surface metallic nanoparticles, whereas the higher Pr surface concentration can be attributed to a certain extent of PrO_x segregation at the support grains [20,44]. An interesting finding is that a significant Na surface concentration was detected for the reduced catalysts whose supports were prepared using NaOH as the precipitating agent (also observed via the intensity of the Na1s XPS peaks in Figure S2), even though the typical washing steps were applied during the material preparation procedures to remove these ions, similarly to other works [22,25,26,45–47]. This can be important during the subsequent

 doi:10.20944/preprints202505.1794.v1

catalytic evaluation of the materials, since Na can potentially act as a catalyst inhibitor (through electronic modifications and inducing a positive charge on Ni) and has often been reported to impair the CO_2 methanation catalytic performance [48–51].

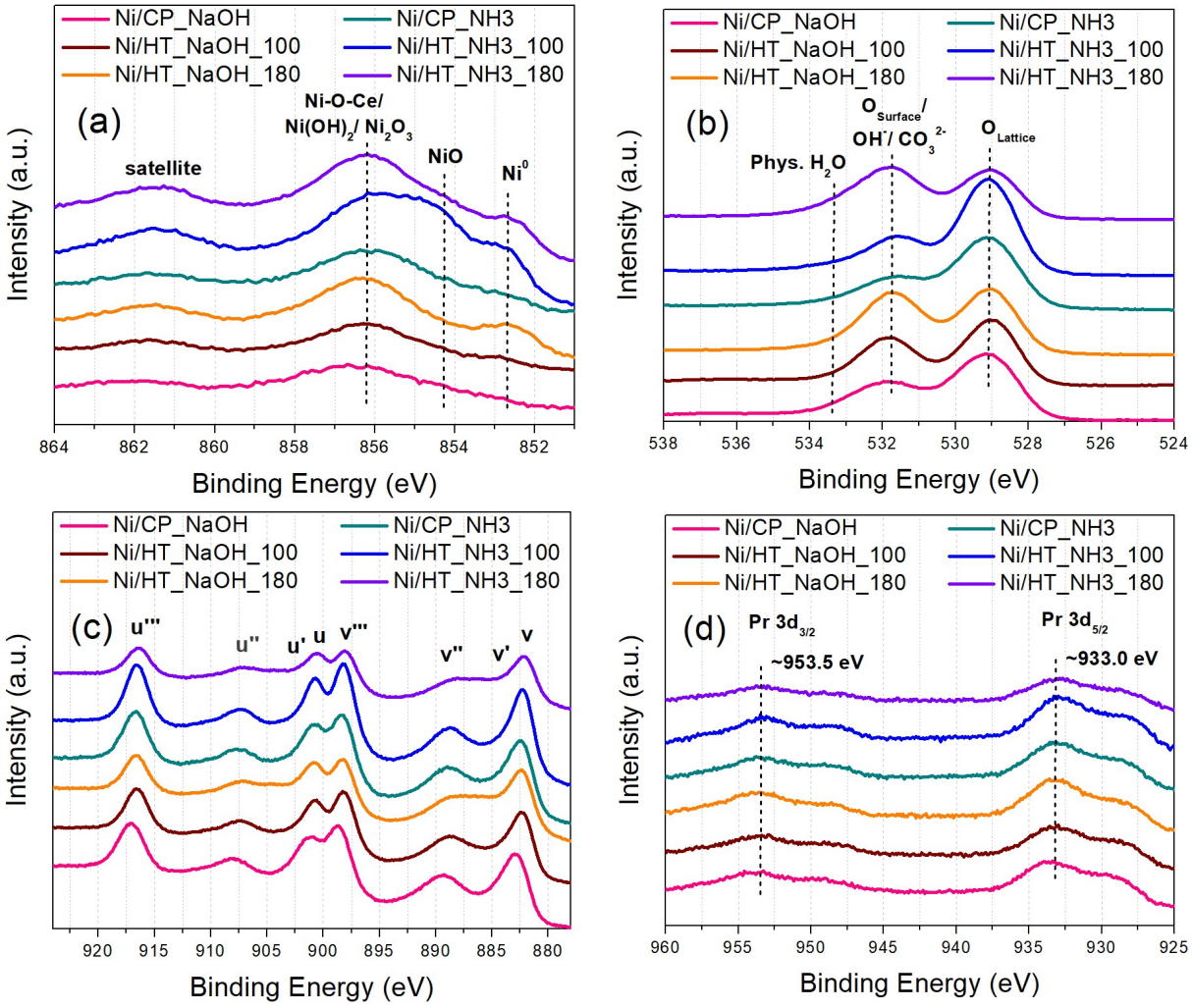

Figure 3. (**a**) Ni2p, (**b**) O1s, (**c**) Ce3d, and (**d**) Pr3d XPS core level spectra for the reduced catalysts.

Lastly, electron microscopy analysis was performed to determine the material nanostructure. TEM images of the reduced Ni-supported catalysts are displayed in Figure 4, whereas the corresponding images of the bare Pr-doped CeO_2 metal oxide supports can be found in Figure S3. The reduced catalysts are comprised of the metal oxide support nanostructure alongside the supported spherical-shaped metallic Ni nanoparticles. The majority of the supported Ni nanoparticles are approx. 5 – 20 nm in diameter (medium-sized), although some of them are quite larger, even up to 50 nm. This size range could be consistent with the average crystallite size of Ni that is calculated via XRD (Table 2), assuming predominantly single-crystal particles. A more accurate estimation of the Ni nanoparticle size via TEM is however challenging, due to the low Z-contrast in the TEM images.

 doi:10.20944/preprints202505.1794.v1

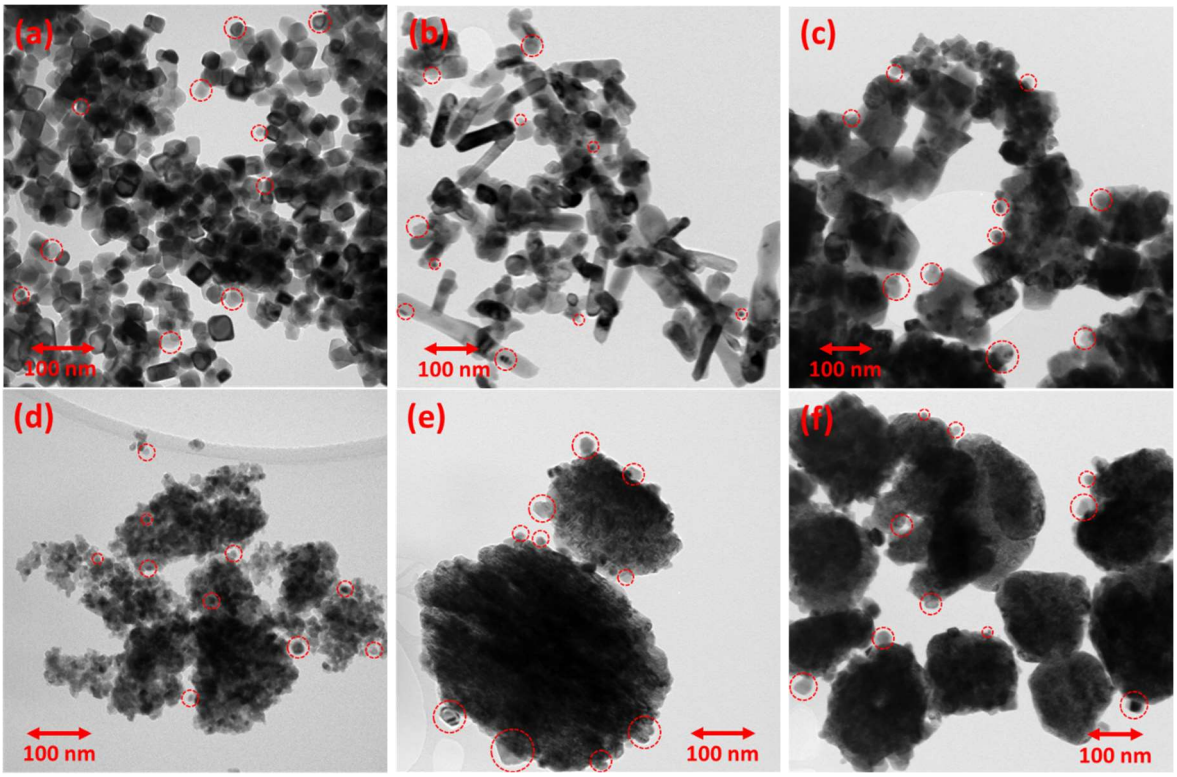

Figure 4. TEM images of the (**a**) Ni/CP_NaOH, (**b**) Ni/HT_NaOH_100, (**c**) Ni/HT_NaOH_180, (**d**) Ni/CP_NH3, (**e**) Ni/HT_NH3_100, and (**f**) Ni/HT_NH3_180 reduced Ni-supported catalysts. The red circles indicate the location of some Ni nanoparticles.

From TEM, it is apparent that the metal oxide support nanostructure changes depending on the synthesis method used to prepare it. Regarding the materials prepared using highly basic NaOH as the precipitating agent, the one with no hydrothermal treatment (i.e., co-precipitation, Ni/CP_NaOH) presents small and rather cubic nanoparticles for the metal oxide support (Figure 4a), whereas the ones with the hydrothermal treatment at 100 and 180 °C (Ni/HT_NaOH_100 and Ni/HT_NaOH_180) present the typical nanostructures of nanorods and nanocubes, respectively (Figure 4b), due to the preferred crystal growth along particular crystalline facets, as is also observed in other literature works [21,22,24,25,46]. For the materials prepared using the mildly basic NH_3-based buffer as the precipitating agent, the one with no hydrothermal treatment (i.e., co-precipitation, Ni/CP_NH3) presents a rather unstructured mesoporous morphology consisting of aggregates of small crystallites (Figure 4d), while the ones with the hydrothermal treatment at 100 and 180 °C (Ni/HT_NH3_100 and Ni/HT_NH3_180) reveal the formation of large particle aggregates for the metal oxide support with a diameter higher than 100 nm. The hydrothermal treatment at 100 °C (Ni/HT_NH3_100) leads to particle aggregates resembling aggregated nanorods, and the hydrothermal treatment at 180 °C (Ni/HT_NH3_180) leads to rather spherical-shaped and polyhedral-shaped particle aggregates (Figure 4e,f).

The TEM images of the bare metal oxide supports, i.e., prior to Ni impregnation/ calcination and reduction, are shown in Figure S3. Nanorods are observed for HT_NaOH_100, nanocubes for HT_NaOH_180, unstructured mesoporous morphology of aggregated crystallites for CP_NH3, and large aggregated particles resembling aggregated nanorods for HT_NH3_100, and spheres/ polyhedra for HT_NH3_180. The notable exception is CP_NaOH, which presents a quite different morphology for the metal oxide support compared to Ni/CP_NaOH. As mentioned during the XRD characterization results, this change/ consolidation in the nanostructure to small cubic nanoparticles followed by crystal growth for Pr-doped CeO_2 occurs during the high-temperature reduction treatment after the Ni impregnation and calcination.

 doi:10.20944/preprints202505.1794.v1

A more precise localization of the metallic Ni supported phase, as well as the determination of the elemental distribution across the materials, are achieved via HAADF-STEM and EDS elemental mapping (Figure 5 and Figure S4). Figure 5 shows the Ni nanoparticle distribution across the catalyst materials, with most of them being medium-sized (5 – 20 nm in diameter), whereas some larger Ni nanoparticles even up to 50 nm in diameter can also be observed. Medium-sized Ni nanoparticles supported over CeO_2-based oxides have been previously reported to be quite efficient during CO_2 methanation [31,47,52]. The Ni nanoparticles are located between the cubic support grains, nanorods, and nanocubes, for the materials prepared with NaOH as the precipitating agent, throughout the unstructured mesoporous support morphology for Ni/CP_NH3, and for Ni/HT_NH3_100 and Ni/HT_NH3_180 they appear to preferentially reside at the outer surface of the large support particle aggregates. The other elements (O, Ce, and Pr) are found to be evenly distributed across the supports, thereby also verifying that Pr (as Pr^{3+}) is solubilized into the CeO_2 lattice. An example of the entire elemental distribution (O, Ce, Pr, and Ni) for Ni/CP_NH3 is shown in Figure S4.

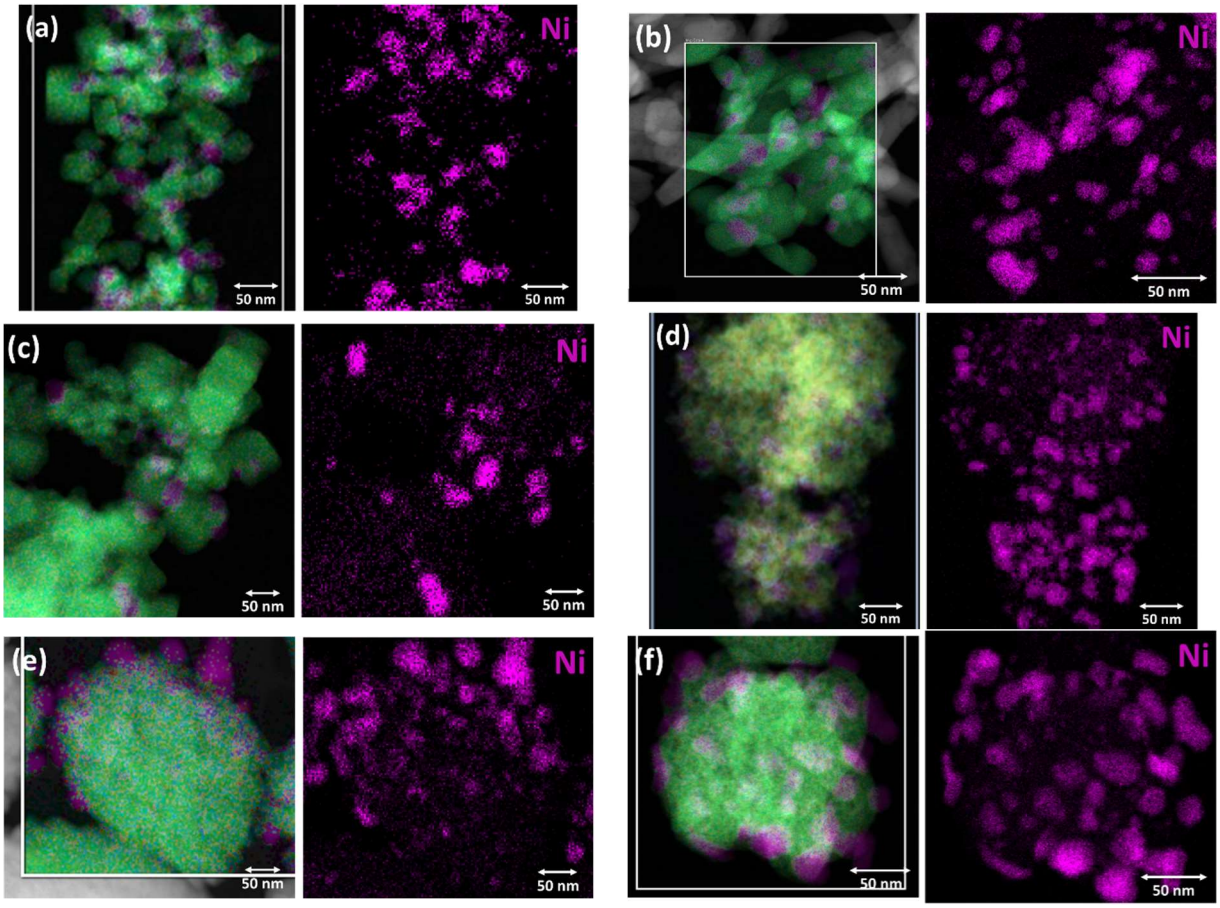

Figure 5. HAADF-STEM EDS elemental mapping images and EDS elemental mapping for Ni of the (**a**) Ni/CP_NaOH, (**b**) Ni/HT_NaOH_100, (**c**) Ni/HT_NaOH_180, (**d**) Ni/CP_NH3, (**e**) Ni/HT_NH3_100, and (**f**) Ni/HT_NH3_180 reduced Ni-supported catalysts.

3.2. Catalytic Activity

The CO_2 methanation catalytic activity was then evaluated as a function of reaction temperature at two different WHSV values, namely at 25,000 ml g_{cat}^{-1} h^{-1} for Experimental Protocol #1, and at 100,000 ml g_{cat}^{-1} h^{-1} for Experimental Protocol #2. During Experimental Protocol #1 (Figure 6), a clear observation regarding the catalytic activity can be made that the materials prepared using mildly basic NH_3-based buffer as the precipitating agent are significantly more active when compared to the materials prepared using highly basic NaOH as the precipitating agent, being able to reach much

 doi:10.20944/preprints202505.1794.v1

higher CO_2 conversion and CH_4 selectivity values at lower reaction temperatures. The corresponding CH_4 yield values are shown in Figure S5a.

Regarding the materials prepared with NaOH as the precipitating agent, the one with no hydrothermal treatment (Ni/CP_NaOH) and the one with the hydrothermal treatment at 100 °C (Ni/HT_NaOH_100) display a similar catalytic activity, whereas the one with the hydrothermal treatment at 180 °C (Ni/HT_NaOH_180) presents a lower one. This is in agreement with other literature works reporting that Ni nanoparticles supported on CeO_2 with nanorod morphology are more active than those supported on CeO_2 with nanocube morphology, which is typically assigned to differences in the oxygen reactivity of the exposed crystalline facets [21–24]. Nevertheless, the significantly inferior catalytic activity of all of these three catalysts compared to those prepared with the NH_3-based buffer as the precipitating agent can be attributed to: i) the lower surface area accompanied by a higher Pr-doped CeO_2 crystallite size, ii) the lower Ni dispersion, and iii) the lower basic site population, especially for the moderately-strong basic sites [31,38]. The significant presence of residual Na on the catalyst surface (Table S1), despite the washing treatments during catalyst preparation, is most probably also responsible for the lower CO_2 conversion and CH_4 selectivity, in agreement with other literature works [48–51].

Regarding the materials prepared with the NH_3-based buffer as the precipitating agent, the ones prepared following hydrothermal treatment at 100 °C (Ni/HT_NH3_100) and 180 °C (Ni/HT_NH3_180), leading to large particle aggregates for the metal oxide support, have a rather similar catalytic activity between them. Overall however, the best catalytic performance, especially at the low-temperature regime, is obtained for the Ni/CP_NH3 material prepared via co-precipitation, leading to a maximum CO_2 conversion of 75% (with 99% CH_4 selectivity) at 350 °C (Table 3). The CO_2 conversion and CH_4 selectivity values then drop at higher temperatures, due to the exothermicity of CO_2 methanation and the promotion of the antagonistic reverse water-gas shift reaction [9]. It is thus found herein, that a rather simple catalyst support (Pr-doped CeO_2) preparation procedure, with an NH_3-based buffer as the precipitating agent and in the absence of hydrothermal treatment, yielding an unstructured mesoporous morphology for the support, leads to an eventually higher CO_2 methanation catalytic activity when compared to the materials prepared using highly basic NaOH and hydrothermal treatments that yield specific, well-defined, catalyst support nanostructures such as nanorods and nanocubes. This can be ascribed to the high specific surface area, high population of basic sites (particularly of moderate strength), favorable Ni dispersion and Ni-support interaction, and the absence of catalyst inhibitors such as residual Na [16,31,38,50].

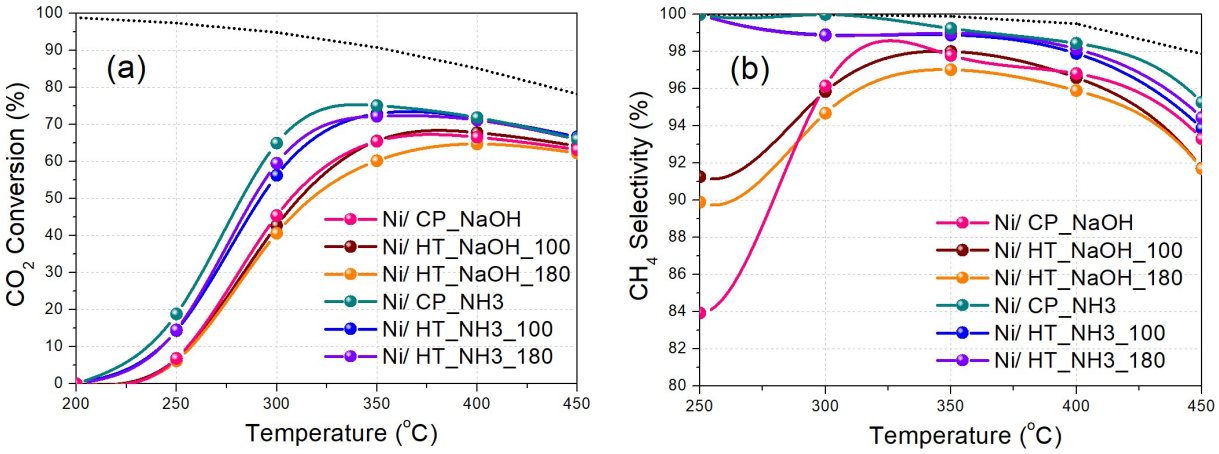

Figure 6. (**a**) CO_2 conversion and (**b**) CH_4 selectivity as a function of reaction temperature (Experimental Protocol #1). The thermodynamic equilibrium (dotted lines) is calculated via Aspen Plus (p = 1 atm and H_2:CO_2 = 4:1).

The catalysts were then evaluated at a higher WHSV of 100,000 ml g_{cat}^{-1} h^{-1} and with additional temperature steps during Experimental Protocol #2 (Figure 7). The increase in the total flow to catalysts weight (F/W) ratio leads to lower CO_2 conversion and CH_4 selectivity values, compared to

 doi:10.20944/preprints202505.1794.v1

the results obtained via Experimental Protocol #1 (higher F/W ratio and lower WHSV) [31,52]. Again, it is found that Ni/CP_NH3 displays the best catalytic performance, with higher CO_2 conversion and CH_4 selectivity values especially at the low-temperature regime, followed by Ni/HT_NH3_180 and Ni/HT_NH3_100. On the other hand, the catalysts prepared with NaOH as the precipitating agent display a substantially inferior CO_2 methanation catalytic performance. The corresponding CH_4 yield values are shown in Figure S5b. The measurements taken for CO_2 conversion values below 20%, and thus at the kinetically controlled regime, allow for the calculation of the activation energy values via the Arrhenius plots (Figure 7c), assuming pseudo-first order reaction kinetics [31]. These values can be found in Table 3 and fall in the range between 90 – 110 kJ/mol, as would be expected for Ni/CeO_2 type catalysts [22,38,53,54].

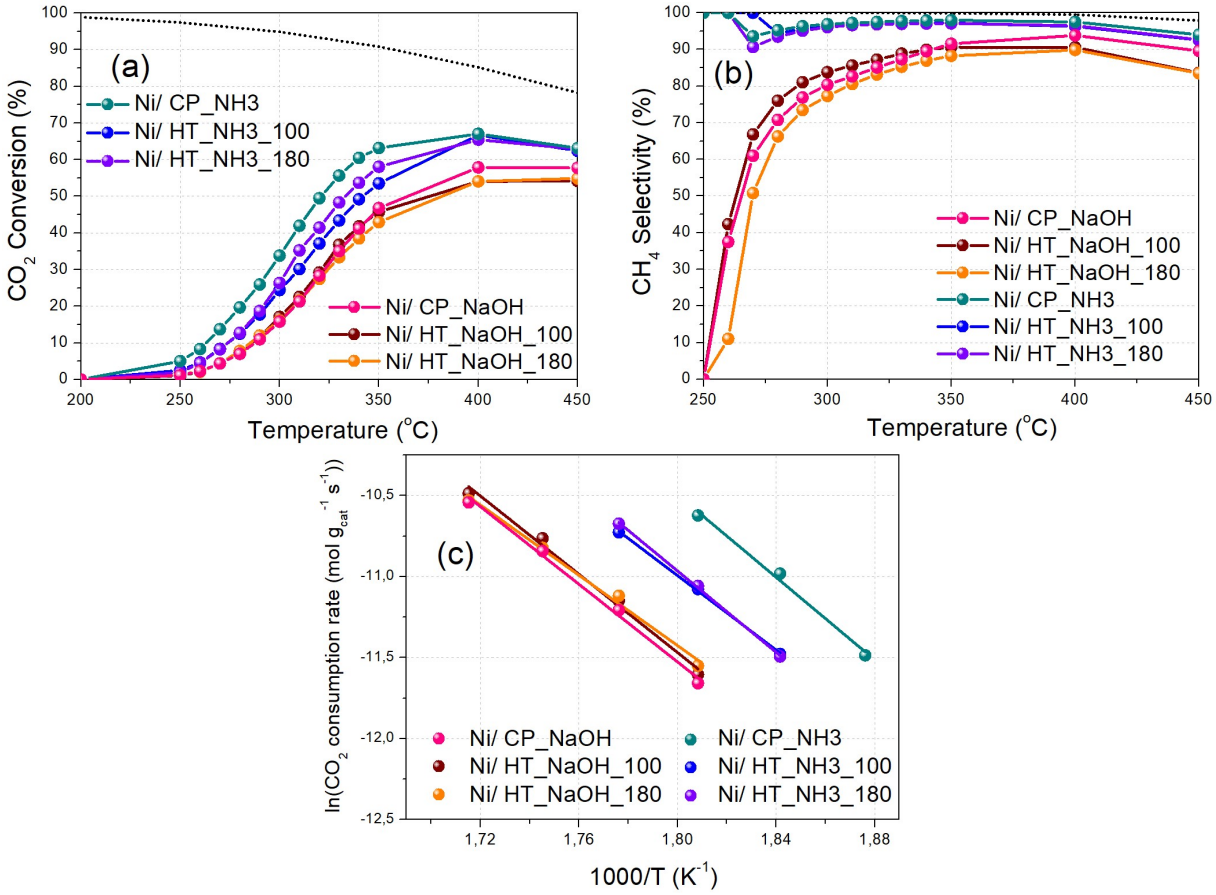

Figure 7. (**a**) CO_2 conversion and (**b**) CH_4 selectivity as a function of reaction temperature (Experimental Protocol #2). (**c**) Arrhenius plots (logarithm of the CO_2 consumption rate vs 1000/T). The thermodynamic equilibrium (dotted lines) is calculated via Aspen Plus (p = 1 atm and H_2:CO_2 = 4:1).

Table 3. CO_2 methanation catalytic performance metrics at 350 °C, and in parenthesis at 300 °C, calculated via Experimental Protocol #1. Activation energy values calculated via Experimental Protocol #2.

Catalyst	CO_2 Conversion (%)	CH_4 Selectivity (%)	CH_4 Yield (%)	Activation Energy (kJ/mol)
Ni/CP_NaOH	65 (45)	98 (96)	64 (44)	101
Ni/HT_NaOH_100	66 (43)	98 (96)	64 (41)	100
Ni/HT_NaOH_180	60 (41)	97 (95)	58 (38)	91
Ni/CP_NH3	75 (65)	99 (100)	75 (65)	106
Ni/HT_NH3_100	73 (56)	99 (99)	72 (56)	95
Ni/HT_NH3_180	72 (59)	99 (99)	72 (59)	104

 doi:10.20944/preprints202505.1794.v1

3.3. Catalytic Stability and Spent Catalyst Characterization

The stability of the best-performing Ni/CP_NH3 catalyst was then evaluated at a constant temperature of 350 °C and WHSV of 25,000 ml g_{cat}^{-1} h^{-1} for a duration of 24 h under Experimental Protocol #3 (Figure 8a). The CO_2 conversion remains quite stable, dropping by just 2% during the entire time-on-stream operation, with a final value of 74%. CH_4 selectivity also remains constant during the time-on-stream duration, at 99%. It is thus shown, that Ni/CP_NH3 can provide a high and stable catalytic performance under long-term operation.

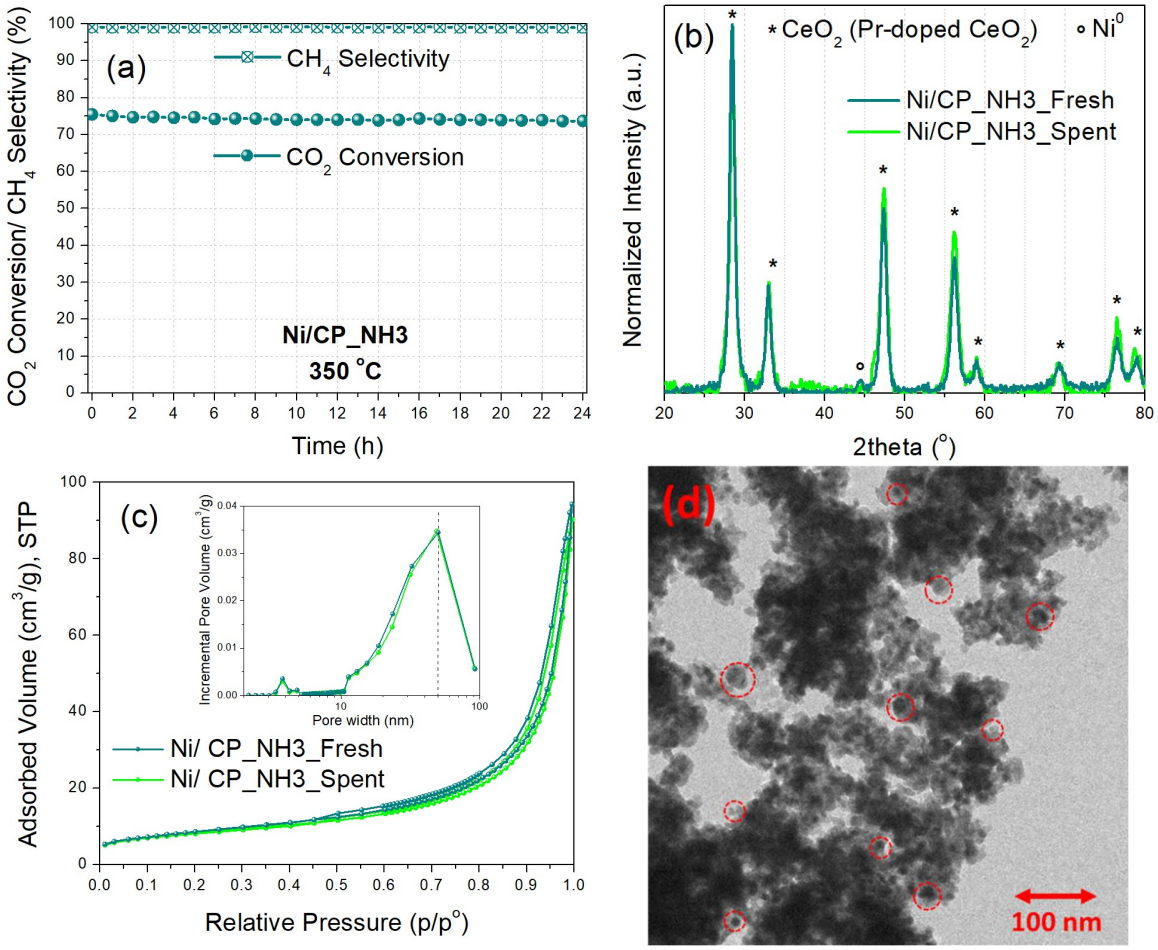

Figure 8. (**a**) Time-on-stream catalytic stability for Ni/CP_NH3 at 350 °C for 24 h (Experimental Protocol #3). (**b**) X-ray diffractograms and (**c**) N_2 physisorption isotherms and pore size distribution graphs (inset) of the fresh (reduced) and spent Ni/CP_NH3 catalysts. (**d**) TEM image of spent Ni/CP_NH3. The red circles indicate the location of some Ni nanoparticles.

The spent Ni/CP_NH3 catalyst following the time-on-stream experiment under Experimental Protocol #3 was then characterized via XRD, N_2 physisorption, and TEM, to examine potential catalyst deactivation effects. The X-ray diffractograms (Figure 8b) of the fresh (reduced) and the spent catalyst largely overlap, showing no significant changes in the catalyst material crystallinity, although the average crystallite size of Ni is now calculated at 13 nm for the spent catalyst, compared to 11 nm for the fresh one. The N_2 physisorption results (Figure 8c) also show similar textural properties for the spent catalyst, with a specific surface area of 29 m^2/g, pore volume of 0.13 cm^3/g, and average pore diameter of 19 nm, i.e., quite similar values to those obtained for the fresh catalyst (Table 2). Furthermore, TEM characterization of the spent Ni/CP_NH3 catalyst (Figure 8d) displays a similar unstructured mesoporous morphology of aggregated small crystallites for the metal oxide support, with medium-sized (5 – 20 nm) supported Ni nanoparticles. Therefore, it can be stated that

 doi:10.20944/preprints202505.1794.v1

Ni/CP_NH3 largely retains its crystallinity, nanomorphology, and Ni dispersion during the time-on-stream operation, with just a potentially minor extent of Ni nanoparticle sintering.

4. Conclusions

This work reports on the co-precipitation and hydrothermal synthesis of Pr-doped CeO_2 support nanostructures for Ni/Pr-CeO_2 CO_2 methanation catalysts by varying the basicity of the precipitating solution and the hydrothermal treatment temperature. It is found that different catalyst support nanostructures can be obtained depending on the support synthesis method, ranging from structured nanorods and nanocubes when using highly basic NaOH and elevated hydrothermal treatment temperature (100 and 180 °C, respectively) to an unstructured mesoporous support morphology consisting of aggregated small crystallites when employing a mildly basic NH_3-based buffer as the precipitating solution in the absence of hydrothermal treatment. In all cases, medium-sized Ni nanoparticles are supported on the metal oxide support nanostructures.

Catalytic activity evaluation showed that the catalysts prepared with the mildly basic NH_3-based buffer as the precipitating agent performed significantly better during CO_2 methanation, with Ni/CP_NH3 synthesized via co-precipitation leading to the best results. On the contrary, the more structured catalyst support nanostructures prepared with highly basic NaOH led to inferior catalytic performance, due to the rather unfavorable physicochemical properties (lower surface area, basic site population of moderate strength, and Ni dispersion), and also due to the catalyst inhibition by residual Na from the synthesis procedure. Furthermore, the best-performing Ni/CP_NH3 catalyst was shown to be highly stable with limited catalyst deactivation during a 24 h time-on-stream experiment.

In short, this study shows that the utilization of rather simpler catalyst support preparation procedures, i.e., co-precipitation in the absence of hydrothermal treatment with the use of a mildly basic precipitating solution, can be more beneficial toward CO_2 methanation when compared to the preparation of highly ordered catalyst support nanostructures, such as with a nanorod or nanocube morphology.

Supplementary Materials: The following supporting information can be downloaded at: Preprints.org. Figure S1: X-ray diffractograms of the calcined Ni-supported catalysts; Table S1: XPS elemental surface concentrations, given in atomic %, and in parentheses in weight %, for the reduced catalysts; Figure S2: Na1s XPS core level spectra of the reduced catalysts, whose supports were synthesized using NaOH as the precipitating agent; Figure S3: TEM images of the (a) CP_NaOH, (b) HT_NaOH_100, (c) HT_NaOH_180, (d) CP_NH3, (e) HT_NH3_100, and (f) HT_NH3_180 calcined metal oxide supports; Figure S4: HAADF-STEM along with EDS elemental mapping for O, Ce, Pr, and Ni of the Ni/CP_NH3 reduced catalyst; Figure S5: CH_4 yield as a function of reaction temperature; (a) Reaction conditions: Experimental Protocol #1; (b) Reaction conditions: Experimental Protocol #2. The thermodynamic equilibrium (dotted lines) is calculated via Aspen Plus (p = 1 atm and H_2:CO_2 = 4:1).

Author Contributions: Conceptualization, A.I.T.; methodology, A.I.T., A.A.D., A.G.S.H., V.S., S.J.H. and M.A.B.; X.X.; validation, A.I.T.; formal analysis, A.I.T., N.D.C., A.A.D., A.G.S.H., V.S. and S.J.H.; investigation, A.I.T., N.D.C., V.S. and M.A.B.; resources, V.S., M.A.B., K.P. and M.A.G..; data curation, A.I.T., A.A.D., A.G.S.H., V.S. and S.J.H.; writing—original draft preparation, A.I.T.; writing—review and editing, N.D.C, V.S., M.A.B., S.M., K.P. and M.A.G..; supervision, M.A.G.; project administration, M.A.G.; funding acquisition, A.I.T., V.S., K.P. and M.A.G.. All authors have read and agreed to the published version of the manuscript.

Funding information: NDC and MAG acknowledge support of this work by the project "Development of new innovative low carbon energy technologies to improve excellence in the Region of Western Macedonia" (MIS 5047197), which is implemented under the Action "Reinforcement of the Research and Innovation Infrastructure" funded by the Operational Program "Competitiveness, Entrepreneurship and Innovation" (NSRF 2014–2020) and co-financed by Greece and the European Union (European Regional Development Fund). AIT thanks the Hellenic Foundation for Research and Innovation (HFRI) for supporting this research work under the 3rd Call for HFRI PhD Fellowships (Fellowship Number: 6033). KP acknowledges financial support from Khalifa University through the grant RC2–2018-024. VS acknowledges funding from project PID2021-127847OB-I00 MCIN/AEI/10.13039/ 501100011033 CIBER-BBN, an initiative funded by the VI National R&D&i Plan 2008–2011, financed by the Instituto de Salud Carlos III and by Fondo Europeo de Desarrollo Regional (Feder) 'Una manera de hacer Europa', with the assistance of the European Regional Development Fund. LMA-ELECMI and NANBIOSIS ICTs are also gratefully acknowledged.

 doi:10.20944/preprints202505.1794.v1

Data availability statement: Dataset available on request from the authors.

Conflicts of interest statement: The authors declare no conflicts of interest.

References

1. Tong, D.; Zhang, Q.; Zheng, Y.; Caldeira, K.; Shearer, C.; Hong, C.; Qin, Y.; Davis, S.J. Committed emissions from existing energy infrastructure jeopardize 1.5 °C climate target. *Nature* **2019**, *572*, 373–377. https://doi.org/10.1038/s41586-019-1364-3.
2. Nong, D.; Simshauser, P.; Binh, D. Greenhouse gas emissions vs CO_2 emissions : Comparative analysis of a global carbon tax. *Appl. Energy* **2021**, *298*, 117223. https://doi.org/10.1016/j.apenergy.2021.117223.
3. Zhao, K.; Jia, C.; Li, Z.; Du, X.; Wang, Y.; Li, J.; Yao, Z. Recent Advances and Future Perspectives in Carbon Capture, Transportation, Utilization, and Storage (CCTUS) Technologies : A Comprehensive Review. *Fuel* **2023**, *351*, 128913. https://doi.org/10.1016/j.fuel.2023.128913.
4. Dziejarski, B.; Krzyżyńska, R.; Andersson, K. Current status of carbon capture, utilization, and storage technologies in the global economy: A survey of technical assessment. *Fuel* **2023**, *342*, 127776. https://doi.org/10.1016/j.fuel.2023.127776.
5. Latsiou, A.I.; Charisiou, N.D.; Frontistis, Z.; Bansode, A.; Goula, M.A. CO_2 hydrogenation for the production of higher alcohols: Trends in catalyst developments, challenges and opportunities. *Catal. Today* **2023**, *420*, 114179. https://doi.org/10.1016/j.cattod.2023.114179.
6. Ozturk, M.; Dincer, I. A comprehensive review on power-to-gas with hydrogen options for cleaner applications. *Int. J. Hydrogen Energy* **2021**, *46*, 31511–31522. https://doi.org/10.1016/j.ijhydene.2021.07.066.
7. Abdalla, A.M.; Hossain, S.; Nisfindy, O.B.; Azad, A.T.; Dawood, M.; Azad, A.K. Hydrogen production, storage, transportation and key challenges with applications: A review. *Energy Convers. Manag.* **2018**, *165*, 602–627. https://doi.org/10.1016/j.enconman.2018.03.088.
8. Liu, Z.; Gao, X.; Wang, K.; Liang, J.; Jiang, Y.; Ma, Q.; Zhao, T.; Zhang, J. A short overview of Power-to-Methane : Coupling preparation of feed gas with CO_2 methanation. *Chem. Eng. Sci.* **2023**, *274*, 118692. https://doi.org/10.1016/j.ces.2023.118692.
9. Tommasi, M.; Naz, S.; Ramis, G.; Rossetti, I. Advancements in CO_2 methanation: A comprehensive review of catalysis, reactor design and process optimization. *Chem. Eng. Res. Des.* **2024**, *201*, 457–482. https://doi.org/10.1016/j.cherd.2023.11.060.
10. Tsiotsias, A.I.; Charisiou, N.D.; Yentekakis, I.V.; Goula, M.A. Bimetallic Ni-based catalysts for CO_2 methanation: A review. *Nanomaterials* **2021**, *11*, 28. https://doi.org/10.3390/nano11010028.
11. Ashok, J.; Pati, S.; Hongmanorom, P.; Tianxi, Z.; Junmei, C.; Kawi, S. A review of recent catalyst advances in CO_2 methanation processes. *Catal. Today* **2020**, *356*, 471–489. https://doi.org/10.1016/j.cattod.2020.07.023.
12. Lv, C.; Xu, L.; Chen, M.; Cui, Y.; Wen, X.; Li, Y.; Wu, C.E.; Yang, B.; Miao, Z.; Hu, X.; et al. Recent Progresses in Constructing the Highly Efficient Ni Based Catalysts With Advanced Low-Temperature Activity Toward CO_2 Methanation. *Front. Chem.* **2020**, *8*, 269. https://doi.org/10.3389/fchem.2020.00269.
13. Alexander, S. Comprehensive review of nickel-based catalysts advancements for CO_2 methanation. **2025**, *207*, 114926. https://doi.org/10.1016/j.rser.2024.114926.
14. Hussain, I.; Tanimu, G.; Ahmed, S.; Aniz, C.U.; Alasiri, H.; Alhooshani, K. A review of the indispensable role of oxygen vacancies for enhanced CO_2 methanation activity over CeO_2-based catalysts: Uncovering, influencing, and tuning strategies. *Int. J. Hydrogen Energy* **2023**, *48*, 24663–24696. https://doi.org/10.1016/j.ijhydene.2022.08.086.
15. Cárdenas-Arenas, A.; Quindimil, A.; Davó-Quiñonero, A.; Bailón-García, E.; Lozano-Castelló, D.; De-La-Torre, U.; Pereda-Ayo, B.; González-Marcos, J.A.; González-Velasco, J.R.; Bueno-López, A. Isotopic and in situ DRIFTS study of the CO_2 methanation mechanism using Ni/CeO_2 and Ni/Al_2O_3 catalysts. *Appl. Catal. B Environ.* **2020**, *265*, 118538. https://doi.org/10.1016/j.apcatb.2019.118538.
16. Zhang, T.; Wang, W.; Gu, F.; Xu, W.; Zhang, J.; Li, Z.; Zhu, T.; Xu, G.; Zhong, Z.; Su, F. Enhancing the low-temperature CO_2 methanation over Ni/La-CeO_2 catalyst: The effects of surface oxygen vacancy and basic site on the catalytic performance. *Appl. Catal. B Environ.* **2022**, *312*, 121385. https://doi.org/10.1016/j.apcatb.2022.121385.

 doi:10.20944/preprints202505.1794.v1

17. Liu, F.; Park, Y.S.; Diercks, D.; Kazempoor, P.; Duan, C. Enhanced CO_2 Methanation Activity of $Sm_{0.25}Ce_{0.75}O_{2-\delta}$-Ni by Modulating the Chelating Agents-to-Metal Cation Ratio and Tuning Metal-Support Interactions. *ACS Appl. Mater. Interfaces* **2022**, *14*, 13295–13304. https://doi.org/10.1021/acsami.1c23881.
18. Siakavelas, G.I.; Charisiou, N.D.; AlKhoori, S.; AlKhoori, A.A.; Sebastian, V.; Hinder, S.J.; Baker, M.A.; Yentekakis, I. V.; Polychronopoulou, K.; Goula, M.A. Highly selective and stable nickel catalysts supported on ceria promoted with Sm_2O_3, Pr_2O_3 and MgO for the CO_2 methanation reaction. *Appl. Catal. B Environ.* **2021**, *282*, 119562. https://doi.org/10.1016/j.apcatb.2020.119562.
19. Siakavelas, G.I.; Charisiou, N.D.; AlKhoori, A.; AlKhoori, S.; Sebastian, V.; Hinder, S.J.; Baker, M.A.; Yentekakis, I. V.; Polychronopoulou, K.; Goula, M.A. Highly selective and stable Ni/La-M (M=Sm, Pr, and Mg)-CeO_2 catalysts for CO_2 methanation. *J. CO_2 Util.* **2021**, *51*, 101618. https://doi.org/10.1016/j.jcou.2021.101618.
20. Tsiotsias, A.I.; Charisiou, N.D.; AlKhoori, A.; Gaber, S.; Stolojan, V.; Sebastian, V.; van der Linden, B.; Bansode, A.; Hinder, S.J.; Baker, M.A.; et al. Optimizing the oxide support composition in Pr-doped CeO_2 towards highly active and selective Ni-based CO_2 methanation catalysts. *J. Energy Chem.* **2022**, *71*, 547–561. https://doi.org/10.1016/j.jechem.2022.04.003.
21. Hashimoto, N.; Mori, K.; Asahara, K.; Shibata, S.; Jida, H.; Kuwahara, Y.; Yamashita, H. How the Morphology of NiO_x-Decorated CeO_2 Nanostructures Affects Catalytic Properties in CO_2 Methanation. *Langmuir* **2021**, *37*, 5376–5384. https://doi.org/10.1021/acs.langmuir.1c00546.
22. Bian, Z.; Chan, Y.M.; Yu, Y.; Kawi, S. Morphology dependence of catalytic properties of Ni/CeO_2 for CO_2 methanation: A kinetic and mechanism study. *Catal. Today* **2020**, *347*, 31–38. https://doi.org/10.1016/j.cattod.2018.04.067.
23. Ma, Y.; Liu, J.; Chu, M.; Yue, J.; Cui, Y.; Xu, G. Enhanced Low-Temperature Activity of CO_2 Methanation Over Ni/CeO_2 Catalyst. *Catal. Letters* **2021**, *152*, 872–882. https://doi.org/10.1007/s10562-021-03677-7.
24. Jomjaree, T.; Sintuya, P.; Srifa, A.; Koo-amornpattana, W.; Kiatphuengporn, S.; Assabumrungrat, S.; Sudoh, M.; Watanabe, R.; Fukuhara, C.; Ratchahat, S. Catalytic performance of Ni catalysts supported on CeO_2 with different morphologies for low-temperature CO_2 methanation. *Catal. Today* **2021**, *375*, 234–244. https://doi.org/10.1016/j.cattod.2020.08.010.
25. Bian, Y.; Xu, C.; Wen, X.; Xu, L.; Cui, Y.; Wang, S.; Wu, C. e.; Qiu, J.; Cheng, G.; Chen, M. CO_2 methanation over the Ni-based catalysts supported on nano-CeO_2 with varied morphologies. *Fuel* **2023**, *331*, 125755. https://doi.org/10.1016/j.fuel.2022.125755.
26. Lin, S.; Li, Z.; Li, M. Tailoring metal-support interactions via tuning CeO_2 particle size for enhancing CO_2 methanation activity over Ni/CeO_2 catalysts. *Fuel* **2023**, *333*, 126369. https://doi.org/10.1016/j.fuel.2022.126369.
27. Nguyen, T.; Long, B.; Anh, P.; Thuy, T.; Nguyen, V.; Anh, C. Nickel/ceria nanorod catalysts for the synthesis of substitute natural gas from CO_2 : Effect of active phase loading and synthesis condition. *J. Sci. Adv. Mater. Devices* **2024**, *9*, 100752. https://doi.org/10.1016/j.jsamd.2024.100752.
28. Yang, W.; Chang, K.; Yang, M.; Yan, X.; Yang, S.; Liu, Y. Facilitating CO_2 methanation over oxygen vacancy-rich Ni/CeO_2 : Insights into the synergistic effect between oxygen vacancy and metal-support interaction. *Chem. Eng. J.* **2024**, *499*, 156493. https://doi.org/10.1016/j.cej.2024.156493.
29. Iglesias, I. Zr promotion effect in CO_2 methanation over ceria-supported nickel catalysts. *Int. J. Hydrogen Energy* **2019**, *44*, 1710–1719. https://doi.org/10.1016/j.ijhydene.2018.11.059.
30. Alcalde-Santiago, V.; Davó-Quiñonero, A.; Lozano-Castelló, D.; Quindimil, A.; De-La-Torre, U.; Pereda-Ayo, B.; González-Marcos, J.A.; González-Velasco, J.R.; Bueno-López, A. Ni/LnO_x Catalysts (Ln=La, Ce or Pr) for CO_2 Methanation. *ChemCatChem* **2019**, *11*, 810–819. https://doi.org/10.1002/cctc.201801585.
31. Tsiotsias, A.I.; Charisiou, N.D.; Harkou, E.; Hafeez, S.; Manos, G.; Constantinou, A.; Hussien, A.G.S.; Dabbawala, A.A.; Sebastian, V.; Hinder, S.J.; et al. Enhancing CO_2 methanation over Ni catalysts supported on sol-gel derived Pr_2O_3-CeO_2: An experimental and theoretical investigation. *Appl. Catal. B Environ.* **2022**, *318*, 121836. https://doi.org/10.1016/j.apcatb.2022.121836.
32. Li, B.; Yuan, X.; Li, B.; Wang, X. Impact of pore structure on hydroxyapatite supported nickel catalysts (Ni/HAP) for dry reforming of methane. *Fuel Process. Technol.* **2020**, *202*, 106359. https://doi.org/10.1016/j.fuproc.2020.106359.

 doi:10.20944/preprints202505.1794.v1

33. Hongmanorom, P.; Ashok, J.; Chirawatkul, P.; Kawi, S. Interfacial synergistic catalysis over Ni nanoparticles encapsulated in mesoporous ceria for CO_2 methanation. *Appl. Catal. B Environ.* **2021**, *297*, 120454. https://doi.org/10.1016/j.apcatb.2021.120454.
34. Cárdenas-Arenas, A.; Quindimil, A.; Davó-Quiñonero, A.; Bailón-García, E.; Lozano-Castelló, D.; De-La-Torre, U.; Pereda-Ayo, B.; González-Marcos, J.A.; González-Velasco, J.R.; Bueno-López, A. Design of active sites in Ni/CeO_2 catalysts for the methanation of CO_2: tailoring the Ni-CeO_2 contact. *Appl. Mater. Today* **2020**, *19*, 100591. https://doi.org/10.1016/j.apmt.2020.100591.
35. Tsiotsias, A.I.; Charisiou, N.D.; Hussien, A.G.S.; Sebastian, V.; Polychronopoulou, K.; Goula, M.A. Integrating capture and methanation of CO_2 using physical mixtures of Na-Al_2O_3 and mono-/ bimetallic (Ru)Ni/Pr-CeO_2. *Chem. Eng. J.* **2024**, *491*, 151962. https://doi.org/10.1016/j.cej.2024.151962.
36. Tsiotsias, A.I.; Charisiou, N.D.; Italiano, C.; Ferrante, G.D.; Pino, L.; Vita, A.; Sebastian, V.; Hinder, S.J.; Baker, M.A.; Sharan, A.; et al. Ni-noble metal bimetallic catalysts for improved low-temperature CO_2 methanation. *Appl. Surf. Sci.* **2024**, *646*, 158945. https://doi.org/10.1016/j.apsusc.2023.158945.
37. Polychronopoulou, K.; Alkhoori, S.; Albedwawi, S.; Alareeqi, S.; Hussien, A.G.S.; Vasiliades, M.A.; Efstathiou, A.M.; Petallidou, K.C.; Singh, N.; Anjum, D.H.; et al. Decoupling the Chemical and Mechanical Strain Effect on Steering the CO_2 Activation over CeO_2-Based Oxides: An Experimental and DFT Approach. *ACS Appl. Mater. Interfaces* **2022**, *14*, 33094–33119. https://doi.org/10.1021/acsami.2c05714.
38. Liu, K.; Xu, X.; Xu, J.; Fang, X.; Liu, L.; Wang, X. The distributions of alkaline earth metal oxides and their promotional effects on Ni/CeO_2 for CO_2 methanation. *J. CO_2 Util.* **2020**, *38*, 113–124. https://doi.org/10.1016/j.jcou.2020.01.016.
39. Liang, C.; Zhang, L.; Zheng, Y.; Zhang, S.; Liu, Q.; Gao, G.; Dong, D.; Wang, Y.; Xu, L.; Hu, X. Methanation of CO_2 over nickel catalysts: Impacts of acidic/basic sites on formation of the reaction intermediates. *Fuel* **2020**, *262*, 116521. https://doi.org/10.1016/j.fuel.2019.116521.
40. López-Rodríguez, S.; Davó-Quiñonero, A.; Bailón-García, E.; Lozano-Castelló, D.; Villar-Garcia, I.J.; Dieste, V.P.; Calvo, J.A.O.; Velasco, J.R.G.; Bueno-López, A. Monitoring by in situ NAP-XPS of active sites for CO_2 methanation on a Ni/CeO_2 catalyst. *J. CO_2 Util.* **2022**, *60*, 101980. https://doi.org/10.1016/j.jcou.2022.101980.
41. Charisiou, N.D.; Siakavelas, G.; Tzounis, L.; Dou, B.; Sebastian, V.; Hinder, S.J.; Baker, M.A.; Polychronopoulou, K.; Goula, M.A. Ni/Y_2O_3–ZrO_2 catalyst for hydrogen production through the glycerol steam reforming reaction. *Int. J. Hydrogen Energy* **2020**, *45*, 10442–10460. https://doi.org/10.1016/j.ijhydene.2019.04.237.
42. D'Angelo, A.M.; Chaffee, A.L. Correlations between Oxygen Uptake and Vacancy Concentration in Pr-Doped CeO_2. *ACS Omega* **2017**, *2*, 2544–2551. https://doi.org/10.1021/acsomega.7b00550.
43. Zhang, X.; Liu, L.; Feng, J.; Ju, X.; Wang, J.; He, T.; Chen, P. Ru Nanoparticles on Pr_2O_3 as an Efficient Catalyst for Hydrogen Production from Ammonia Decomposition. *Catal. Letters* **2022**, *152*, 1170–1181. https://doi.org/10.1007/s10562-021-03709-2.
44. Borchert, H.; Frolova, Y. V.; Kaichev, V. V.; Prosvirin, I.P.; Alikina, G.M.; Lukashevich, A.I.; Zaikovskii, V.I.; Moroz, E.M.; Trukhan, S.N.; Ivanov, V.P.; et al. Electronic and chemical properties of nanostructured cerium dioxide doped with praseodymium. *J. Phys. Chem. B* **2005**, *109*, 5728–5738. https://doi.org/10.1021/jp045828c.
45. Li, L.; Jiang, L.; Li, D.; Yuan, J.; Bao, G. Enhanced low-temperature activity of CO_2 methanation over Ni/CeO_2 catalyst : Influence of preparation methods. *Appl. Catal. O Open* **2024**, *192*, 206956. https://doi.org/10.1016/j.apcato.2024.206956.
46. Lin, S.; Tang, R.; Liu, X.; Gong, L.; Li, Z. Modulating CO_2 methanation activity on Ni/CeO_2 catalysts by tuning ceria facet-induced metal-support interaction. *Int. J. Hydrogen Energy* **2024**, *51*, 462–475. https://doi.org/10.1016/j.ijhydene.2023.10.095.
47. Varvoutis, G.; Lykaki, M.; Stefa, S.; Binas, V.; Marnellos, G.E.; Konsolakis, M. Deciphering the role of Ni particle size and nickel-ceria interfacial perimeter in the low-temperature CO_2 methanation reaction over remarkably active Ni/CeO_2 nanorods. *Appl. Catal. B Environ.* **2021**, *297*, 120401. https://doi.org/10.1016/j.apcatb.2021.120401.

 doi:10.20944/preprints202505.1794.v1

48. Tsiotsias, A.I.; Charisiou, N.D.; Yentekakis, I.V.; Goula, M.A. The role of alkali and alkaline earth metals in the CO_2 methanation reaction and the combined capture and methanation of CO_2. *Catalysts* **2020**, *10*, 812. https://doi.org/10.3390/catal10070812.
49. Le, T.A.; Kim, T.W.; Lee, S.H.; Park, E.D. Effects of Na content in Na/Ni/SiO_2 and Na/Ni/CeO_2 catalysts for CO and CO_2 methanation. *Catal. Today* **2018**, *303*, 159–167. https://doi.org/10.1016/j.cattod.2017.09.031.
50. Wu, H.C.; Chen, T.C.; Wu, J.H.; Pao, C.W.; Chen, C.S. Influence of sodium-modified Ni/SiO_2 catalysts on the tunable selectivity of CO_2 hydrogenation: Effect of the CH_4 selectivity, reaction pathway and mechanism on the catalytic reaction. *J. Colloid Interface Sci.* **2021**, *586*, 514–527. https://doi.org/10.1016/j.jcis.2020.10.117.
51. Beierlein, D.; Häussermann, D.; Pfeifer, M.; Schwarz, T.; Stöwe, K.; Traa, Y.; Klemm, E. Is the CO_2 methanation on highly loaded Ni-Al_2O_3 catalysts really structure-sensitive? *Appl. Catal. B Environ.* **2019**, *247*, 200–219. https://doi.org/10.1016/j.apcatb.2018.12.064.
52. Du, Y.; Qin, C.; Xu, Y.; Xu, D.; Bai, J.; Ma, G.; Ding, M. Ni nanoparticles dispersed on oxygen vacancies-rich CeO_2 nanoplates for enhanced low-temperature CO_2 methanation performance. *Chem. Eng. J.* **2021**, *418*. https://doi.org/10.1016/j.cej.2021.129402.
53. Luisetto, I.; Stendardo, S.; Senthil Kumar, S.M.; Selvakumar, K.; Kesavan, J.K.; Iucci, G.; Pasqual Laverdura, U.; Tuti, S. One-pot synthesis of $Ni_{0.05}Ce_{0.95}O_{2-\delta}$ catalysts with nanocubes and nanorods morphology for CO_2 methanation reaction and in operando DRIFT analysis of intermediate species. *Processes* **2021**, *9*, 1899. https://doi.org/10.3390/pr9111899.
54. Lin, S.; Hao, Z.; Shen, J.; Chang, X.; Huang, S.; Li, M.; Ma, X. Enhancing the CO_2 methanation activity of Ni/CeO_2 via activation treatment-determined metal-support interaction. *J. Energy Chem.* **2021**, *59*, 334–342. https://doi.org/10.1016/j.jechem.2020.11.011.